



Effect of C content and annealing on dendrite structure evolution and corrosion resistance of CoCrFeMnNi alloys



Fucheng Zhu^a, Changjun Wu^{a,b,*}, Ya Liu^{a,b}, Haoping Peng^{a,b}, Xiangying Zhu^{a,b}, Xuping Su^{a,b}

^a Jiangsu Key Laboratory of Materials Surface Science and Technology, School of Materials Science and Engineering, Changzhou University, Changzhou 213164, China

^b Jiangsu Collaborative Innovation Center of Photovoltaic Science and Engineering, Changzhou University, Changzhou 213164, China

ARTICLE INFO

Keywords:

High-entropy alloys
Carbon alloying
Annealing treatment
Microstructure
Corrosion resistance

ABSTRACT

In this study, a series of CoCrFeMnNiC_x (0–0.8 at% C) high-entropy alloys (HEAs) were prepared by vacuum arc melting and subsequently vacuum annealed at 800°C or 1000°C for 120 h. The aim was to investigate the microstructure evolution and corrosion behavior of the as-cast and annealed CoCrFeMnNiC_x alloys in a neutral corrosion solution. Experimental results revealed that the addition of C can refine the as-cast dendrite structure, with an optimal C content of 0.4 at%. Annealing treatment led to a decrease in C solubility in the face-centered cubic (FCC) phase, resulting in the precipitation of carbides. In a 3.5 wt% NaCl neutral solution, the as-cast alloy containing 0.4 at% C exhibited the highest corrosion resistance. After annealing at 1000°C, the alloy's pitting potential and corrosion resistance were further improved. The corrosion behavior of both the as-cast and annealed CoCrFeMnNiC_x alloys was primarily composed of pitting and intergranular corrosion, although the dominant mechanism varied among these alloys. This study establishes a correlation between microstructure evolution and corrosion behavior, providing insights for the design of high-entropy alloys with superior corrosion resistance.

1. Introduction

High entropy alloys (HEAs)^[1] contain high concentrations of multiple significant elements, and in most cases, they form single-phase solid solutions. Their high entropy effect, lattice distortion effect, slow diffusion effect, and "cocktail" effect^[2] greatly expand the development and application of HEAs. The equiaxed CoCrFeMnNi alloy is FCC single phase, one of the widely studied HEAs^[3–6]. CoCrFeMnNi alloys have excellent fracture toughness^[3,4] and corrosion resistance^[5,6] at low and room temperatures. Compared with multiphase HEAs, single-phase CoCrFeMnNi alloys generally have lower strength and hardness^[7,8] and better corrosion resistance^[9–11].

It is well known that the corrosion resistance of alloys depends on the alloying elements, microstructure, and so on. Both CoCrFeMnNi alloy and austenitic stainless steel contain Cr and Ni elements, which benefit corrosion resistance, but their microstructures differ. Different microstructures can lead to other corrosion behavior. Luo et al.^[12] found that the passive film on 304 L stainless steel mainly comprises Cr₂O₃, while the passive film on CoCrFeMnNi alloy is rich in Fe, Mn, and many metal hydroxides. Different element ratios also affect the corrosion behavior of the alloy. Aiso et al.^[13] found that Cr makes CoCrFeMnNi

alloy passivated in a corrosive solution. Adding Co and Fe can reduce the passivation current density and advance the passivation behavior. Ni can inhibit the active dissolution of the alloy surface during corrosion, while Mn can increase the active dissolution rate. With increased Cr content, the pitting corrosion resistance and passivation ability of CoCrFeMnNi alloy are improved, which is related to the enrichment of Cr in the passivation film^[14–16]. At the same time, the low hardness and strength of single-phase CoCrFeMnNi HEA also limit its industrial application.

Interstitial atoms C, N, and B greatly affect the solution and precipitation strengthening of the alloy^[17–20]. The atomic radius of C is less than 0.1 nm, which can directly enter the lattice gap and improve the strength of the alloy through solid solution strengthening. Or it can combine with Cr, Fe, and other elements in the matrix to produce carbides at the grain boundaries or inside the grains and improve the mechanical properties of the alloy by grain refining or precipitation strengthening^[21–23]. It is one of the most commonly used interstitial atoms in alloy strengthening. Several studies have shown that the C-alloyed CoCrFeMnNiC_x HEAs have a dual phase structure consisting of FCC phase and M₇C₃ carbide (or M₂₃C₆ carbide) phase. With the increase of C content, the volume fraction of the carbide phase also

* Corresponding author.

E-mail address: wucj@cczu.edu.cn (C. Wu).

increases [24–27]. The carbide phase increases with the growth of carbon content. Although the dual-phase structure can significantly improve the hardness of the alloy [22], the potential difference between the precipitated carbide and the FCC matrix phase makes it easy to form a micro-corrosion battery, worsening the corrosion resistance of the alloy. It is found that the addition of an appropriate amount of C has a positive effect on the corrosion resistance of CoCrFeMnNi alloy [28–31]. In 3.5 wt% NaCl-saturated Ca(OH)₂ solution, 0.5 at% C can improve the pitting corrosion resistance of CoCrFeMnNi alloy. At this time, Cr and Co elements were enriched in the passive film [29]. In 0.05 M HCl solution, the non-obvious oxidation of C promotes the formation of the Mn-enriched oxide layer and improves the corrosion resistance of CoCrFeMnNi HEA films [30].

In summary, there is much research on C atoms in HEAs. In acidic and alkaline solutions, the addition of C has a positive effect on the corrosion resistance of the alloy. Some studies also analyzed the microstructure and mechanical properties changes after adding the C element. However, the influence mechanism of C on the corrosion behavior of CoCrFeMnNi alloy in a neutral corrosion solution is still unclear.

This paper shows the microstructure and corrosion behavior of CoCrFeMnNi alloy with different carbon content in 3.5 wt% NaCl solution was studied by optical microscopy (OM), scanning electron microscopy (SEM), electrochemical impedance spectroscopy (EIS), and potentiodynamic polarization curve. Besides, the elements and types of corrosion products on the alloy surface were characterized by an energy dispersive spectrometer (EDS) and Raman spectrometer. The mechanism of the effect of C on the microstructure evolution of CoCrFeMnNi alloy was studied, and the relationship between the change of C and microstructure and the corrosion resistance of the alloy was clarified.

2. Materials and methods

High-purity metal Co, Cr, Fe, Mn, and Ni particles with a purity of 99.99 wt% and Fe-5 wt% C intermediate alloy were used as raw materials. A series of CoCrFeMnNiC_x (0–0.8 at% C) alloys, named C00, C02, C04 and C08, were prepared by vacuum arc melting in a high-purity argon atmosphere. Each ingot was melted four times to ensure uniform composition and cooled to room temperature in a water-cooled copper mold. The cooled alloy ingots were cut into 10 mm × 10 mm × 2 mm sheets by wire-cut electrical discharge machining. The analysis of carbon content in each alloy was performed by LECO CS844 Elemental Analyzer. A polished sample with 1 g was placed into the high-frequency furnace for combustion. The results are summarized in Table 1. After grinding off the surface cutting layer, the alloy sheets were individually sealed in vacuum quartz tubes and then annealed at 800°C and 1000°C for 120 h, respectively. The annealed alloys were quenched in cold water at the end of treatment.

The alloys were polished with 400 #, 800 #, 1000 #, and 2000# sandpaper and then polished to a mirror surface by a polishing machine. The phase composition of the as-cast and annealed HEAs was analyzed by a D/max 2500PC X-ray diffraction (XRD). Cu-K_α Ray was used to scan at the speed of 0.4 °/min in the range of 10° ~ 90°. JSM-6510 scanning electron microscope (SEM) and Oxford energy dispersive spectrometer (EDS) were used to observe the microstructure and analyze the composition of HEAs. A 20 kV accelerating voltage and 15 mm working

distance was used. As for the metallographic observation, the samples were etched by CuSO₄: HCl: 1–3 H₂O solution. The residual corrosion solution on the surface was cleaned with alcohol and dried, and the microstructure was observed with a Leica DMI 3000 optical microscope. To obtain the grain size and orientation relationship of HEAs, electron backscatter diffraction (EBSD, OXFORD NordlysNao) further examined some critical samples. The step size was set to 0.6 μm and the sample was tilted at an angle of 70°.

The electrochemical tests of the as-cast and annealed CoCrFeMnNiC_x alloys in 3.5 wt% NaCl solution was measured by PARSTAT 4000 A instrument. All measurements were carried out in a conventional three-electrode electrolytic cell. The platinum plate was used as the auxiliary electrode, and the saturated calomel electrode (SCE) was used as a reference electrode. The as-cast and partially annealed CoCrFeMnNiC_x alloys were used as the working electrode with an exposed area of 1 cm². It was immersed in 3.5 wt% NaCl solution without stirring for 2 h. After soaking, the samples were tested by open circuit potential (OCP) for the 1800 s. After reaching the steady state, EIS was carried out in the frequency range of 10⁻²–10⁵ Hz. The voltage scanning range of the potentiodynamic polarization test was –0.5 - +0.5 (vs. OCP), and the scanning rate was 0.5 mV/s. All electrochemical measurements were repeated 3 times under the same conditions. The curve presented in this paper is the one closest to the average result. The surface morphology of the alloys tested by potentiodynamic polarization curve was observed by Leica DMI 3000 optical microscope.

In the immersion experiment, 3.5 wt% NaCl solution was prepared with deionized water, and the as-cast alloys were immersed in the solution for 30 d under natural ventilation. JSM-6510 scanning electron microscope (SEM) was used to observe the corrosion morphology of the alloys. The composition of the corrosion product was analyzed through EDS and Raman spectroscopy. The Raman shift range was 0–2000 cm⁻¹ and the spectrum capture time was 30 s.

3. Results

3.1. Microstructure evolution and phase constituent

3.1.1. Microstructure observation

The OM images of the as-cast CoCrFeMnNiC_x alloys are show in Fig. 1. All the as-cast alloys are composed of dendrite structure, which changed with C content. As can be seen in Fig. 1a₁, the orientation of the network dendritic structure is random, and many secondary dendrites exist. With the increase of C content, the dendrites in the as-cast C04 alloy are significantly refined, the secondary dendrites are staggered, and the dendrites are closely combined, as shown in Fig. 1c₁. The observation of abnormally coarse secondary dendrites in the C08 alloy (Fig. 1d₁), along with the slender dendrite trunk and thick and short secondary dendrites, suggests that the increased carbon content has an influence on the microstructure of the alloy. The interface between the dendrites becomes more apparent, indicating a change in the dendrite morphology. From the absence of precipitates in the as-cast alloy, it can be inferred that the added carbon is dissolved into the FCC matrix. This increase in carbon content may have an impact on the nucleation and growth behavior of the dendrites, leading to changes in their morphology and spacing. The slightly larger dendrite spacing observed in the C08 alloy, compared to the C00 alloy, could be attributed to the presence of carbon in solid solution, which may affect dendrite growth kinetics. Overall, these observations provide insights into the microstructural changes resulting from the increased carbon content in the CoCrFeMnNiC_x alloys.

After annealing at 800 °C, the microstructure of the C00 alloy underwent significant changes. As shown in Fig. 1a₂, the dendrites that were present during solidification disappeared and transformed into equiaxed crystals, which indicates a complete recrystallization process. In the C02 alloy, consisting of a higher carbon content, the driving energy for grain growth increases. As a result, the grains grow into long

Table 1
Contents of carbon in the as-cast alloys.

Alloys	Nominal C content		Detected C content
	at%	wt%	
C00	-	-	-
C02	0.2	0.043	0.056
C04	0.4	0.086	0.094
C08	0.8	0.173	0.192

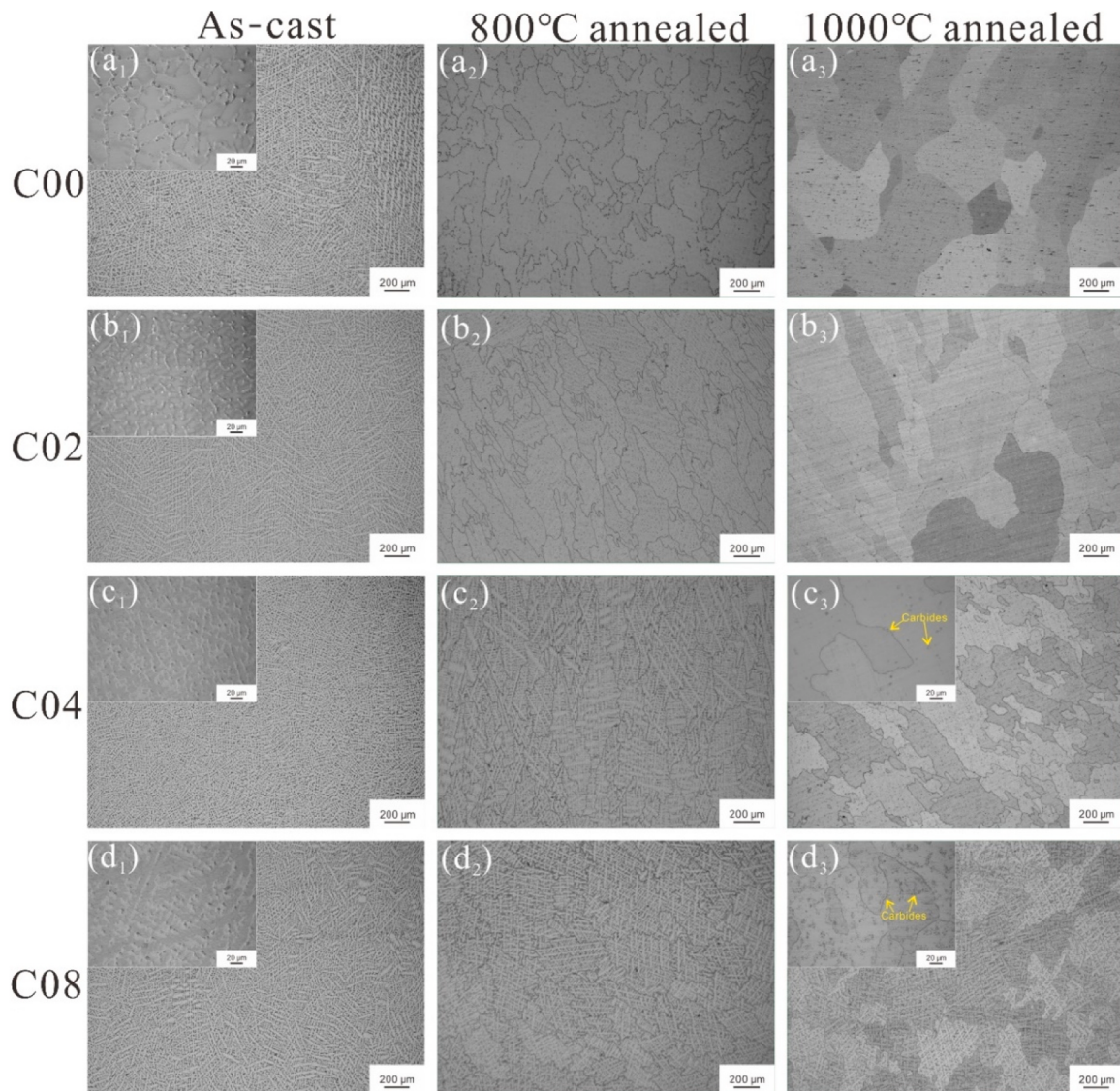


Fig. 1. OM images of the as-cast and annealed CoCrFeMnNiCx alloys. (a₁-a₃) C00 alloy; (b₁-b₃) C02 alloy; (c₁-c₃) C04 alloy; (d₁-d₃) C08 alloy. The first, second and last columns are related to the as-cast state, 800°C annealed state and 1000°C annealed state, respectively.

strips of equiaxed grains, with faintly visible subgrains inside. This is depicted in Fig. 1b₂. Moving on to the C04 alloy shown in Fig. 1c₂, the microstructure consists of massive equiaxed grains. However, there are still some undescended dendrites observed within the grains. This suggests that the complete transformation to solely equiaxed grains has not yet been achieved in this alloy. In the case of the C08 alloy, as shown in Fig. 1d₂, the microstructure also comprises equiaxed grains, but with zigzag grain boundaries. Compared to the C04 alloy in Fig. 1c₂, the dendrites are more compact within the grains.

After annealing at 1000°C, further changes are observed in the microstructures of these alloys. In the C00 and C02 alloys, the subgrains within the grains completely disappear, as depicted in Figs. 1a₃ and 1b₃. In the C04 alloy, the residual dendrites that were observed in the equiaxed grains during annealing at lower temperatures also disappear. However, dense dots are now visible within the grains. Upon closer examination in the local detail diagram, these dots are identified as precipitated point carbides. The carbides within the grains appear as dots, while those located at the grain boundaries take on a strip-shaped appearance. Additionally, the average size of the carbides is larger than that of the grains themselves, as shown in Fig. 1c₃. In the C08 alloy, a similar phenomenon is seen to the one observed after annealing at

800°C. The residual dendrite structure in the equiaxed grains has improved, indicating partial recrystallization. However, there is a significant presence of carbides precipitated in the grain boundaries and interdendritic region, as shown in Fig. 1d₃.

3.1.2. Phase constituent

Fig. 2 shows the XRD patterns of the as-cast and annealed CoCrFeMnNiCx alloys. In the as-cast alloys, no carbide peak was detected when 0.8 at% C was added, indicating that the carbon completely dissolved in the FCC matrix phase. The Fig. 2a₂ shows a left shift in the FCC (111) peak with increasing carbon content, indicating an increase in lattice parameters. The lattice constants were determined to be 3.5950 Å, 3.5978 Å, 3.5983 Å, and 3.6001 Å for the respective alloys. This shift suggests that the presence of more carbon atoms results in increased lattice constants.

After annealing at 800°C or 1000°C, weak M₇C₃ carbide peaks were detected in the C04 and C08 alloys, as shown in Fig. 2b₂ and Fig. 2c₂. This observation is consistent with Ref. [24,32]. Interestingly, in the C04 alloy, weak carbide peaks were detected in the 1000°C annealed alloy but not in the 800°C annealed alloy, indicating the significant influence of annealing temperature on carbide formation.

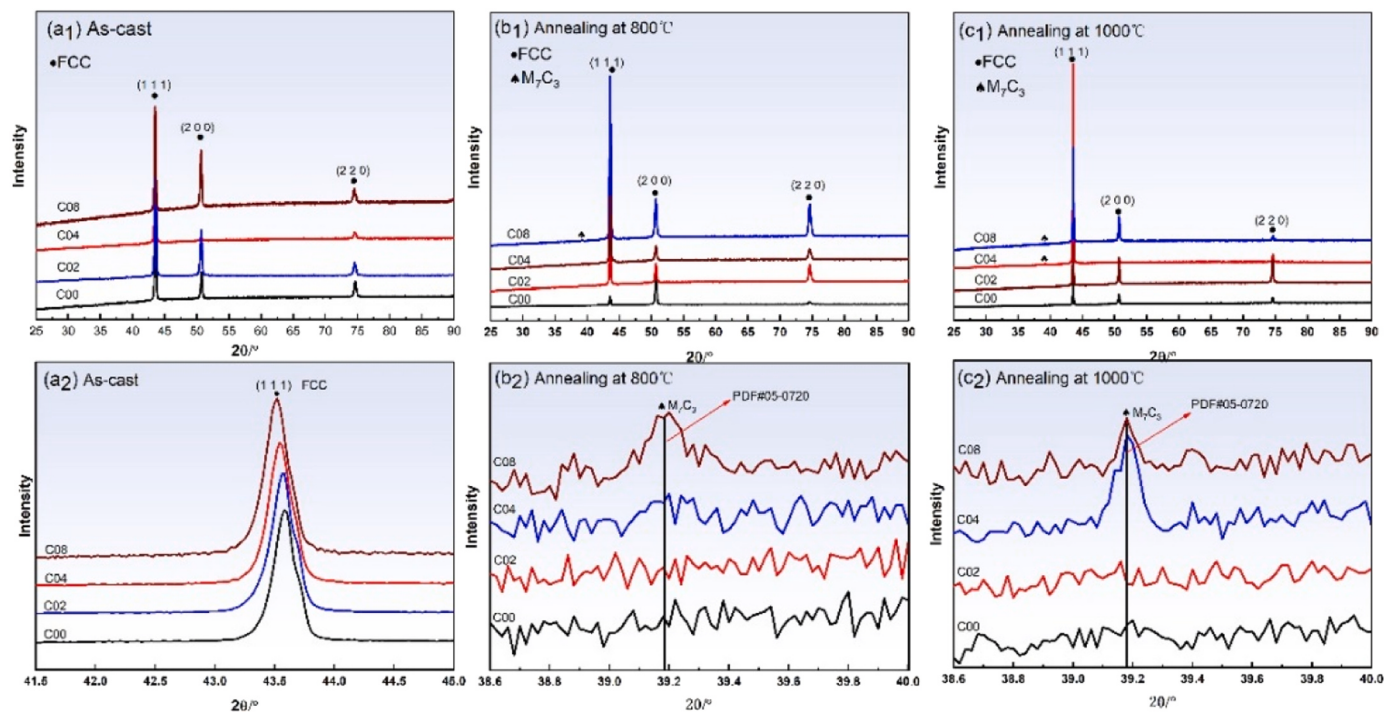


Fig. 2. XRD patterns of the CoCrFeMnNiC_x HEA. (a₁) as-cast alloys; (a₂) enlarged 41.5–45.0° part of image (a₁); (b₁) 800°C annealed alloys; (b₂) enlarged 38.6°–40.0° part of image (b₁); (c₁) 1000°C annealed alloys; (c₂) enlarged 38.6°–40.0° part of image (c₁).

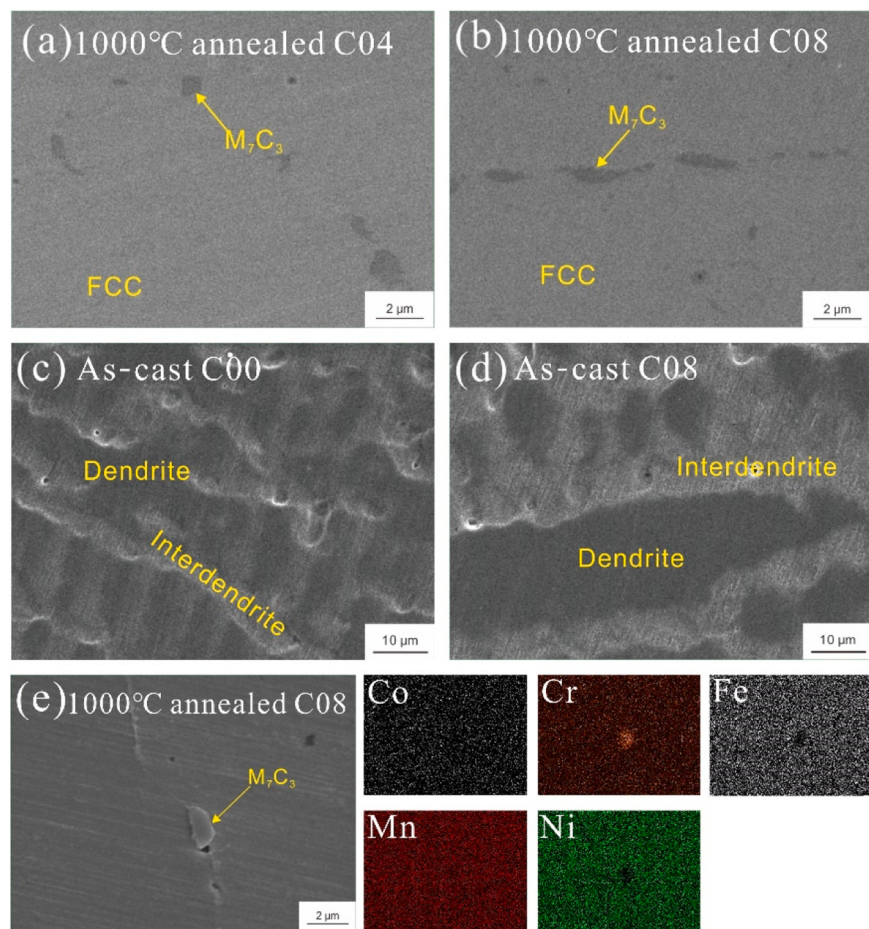


Fig. 3. SEM images of some selected CoCrFeMnNiC_x alloys. (a) 1000°C annealed C04; (b) 1000°C annealed C08; (c) as-cast C00; (d) as-cast C08; (e) EDS mapping of the 1000°C annealed C08.

As shown in Figs. 3a, 3b, dark gray precipitates in strip and granular forms can be observed on the FCC matrix. SEM-EDS results in Table 2 and EDS elemental mapping in Fig. 3e indicate that the precipitates are enriched in Cr, while their Co and Ni content is less than 3 at%. The ratio of C/(Cr+Mn+Fe) is close to 3:7. Combining the XRD results, the available reference [25], and TEM studies from previous works [21,24, 33], it is concluded that the precipitated phase is M₇C₃ carbide. The size of the carbides appears to be closely related to the carbon content, with scattered point-like distribution in the C04 alloy (Fig. 3a) and strip-like distribution in the C08 alloy (Fig. 3b). Although TEM tests were not performed in the present work, we refer to previous studies [21,24,25, 33] that confirm the presence of M₇C₃ carbide using XRD, OM, and EDS analysis. Anyway, the focus of the present work is on the evolution of microstructure morphology and the influence of carbides and microstructure morphology on corrosion behavior.

From Table 2, it can be observed that there is a compositional difference between dendrites and the interdendritic regions. Cr, Fe, and Co elements are enriched in the dendrites of the alloy, while Mn and Ni elements are enriched in the interdendritic regions. The addition of C does not alter the element segregation phenomenon in the as-cast alloy [27].

3.1.3. Grain orientation and grain boundary distribution

After annealing at 1000°C, some sub-grain residues are still evident in the C08 alloy. To gather more detailed information about the microstructure, an EBSD test was conducted, and the results are presented in Fig. 4. Fig. 4a shows that the C08 alloy consists of FCC grains with a small amount of carbide precipitation. The carbides that precipitate at the grain boundaries are clustered together, forming elongated red grains. Fig. 4b illustrates that the FCC grains do not exhibit a clear preferred orientation, and grains of the same color can be observed in certain regions, indicating that grain boundary migration has severed dendrites during their growth into equiaxed grains. Most grains exhibit subtle color variations, indicating differences in sub-grain orientations. This agrees with the observations in Fig. 1d₃.

The low-angle grain boundaries (marked by black lines) and high-angle grain boundaries (marked by red lines) are identified in Fig. 4c. The low-angle grain boundaries correspond to the boundaries with slight color differences in Fig. 4b, suggesting that there is only a small orientation difference between sub-grains. Specifically, only the grain boundaries with an orientation difference of 2°~15° are classified as low-angle grain boundaries. As seen from Fig. 4d, the regions with sub-crystals and precipitates within the grains have a higher degree of misorientation, indicating a higher density of defects in those areas.

3.2. Corrosion resistance of the CoCrFeMnNiC_x alloys

As presented above, the microstructure of the as-cast C04 alloy was observed to be refined, with closely bonded dendrites. This refined microstructure is beneficial as it reduces the susceptibility to intergranular corrosion [34], thereby enhancing corrosion resistance. To further investigate the impact of annealing temperature on the corrosion resistance of CoCrFeMnNiC_x alloys, the corrosion resistance of the C04

alloy was examined in various states.

3.2.1. Potentiodynamic polarization measurements

The potentiodynamic polarization curves in Fig. 5 show that all samples, including the as-cast alloys with different carbon contents and the annealed C04 alloys, exhibit passivation in the 3.5 wt% NaCl solution, which is consistent with the research results of Luo et al. [29]. In potentiodynamic polarization curves, the anode region represents the dissolution process of the working electrode. In contrast, the cathode region represents the oxygen diffusion process of the oxygen absorption reaction [35]. The O²⁻ dissolved in the electrolyte reacts with H₂O to form OH⁻, and the metal cations on the sample surface bind to OH⁻, comprising metal oxides and hydroxides deposited on the alloy surface. Adding carbon to the as-cast alloys increased the width of the anodic passivation zone, indicating an improvement in pitting corrosion resistance. Similarly, annealing at 800°C and 1000°C further increased the width of the passivation zone (Fig. 5c), suggesting enhanced corrosion resistance. The corrosion current density corresponding to -0.25 Vsce was chosen as the passivation current density for each alloy. The pitting potential and passivation current density are summarized in Figs. 5b and 5d.

The as-cast C04 alloy demonstrated the lowest dimensional passivation current density and the highest pitting potential, which could be attributed to its refined microstructure. The E_p-E_{corr} value, representing pit nucleation resistance [36], was larger for the C04 alloy annealed at 1000°C, indicating improved resistance to pit formation. That is to say, annealing treatment improves the pit nucleation resistance.

Table 3 shows the fitted parameters of the polarization curves. The corrosion current density, which serves as a measure of corrosion resistance, was found to be the lowest for the as-cast C04 alloy among all the as-cast alloys. Notably, the C04 alloy annealed at 1000°C exhibited the best corrosion resistance according to the polarization curve fitting results.

The surface morphology of the as-cast CoCrFeMnNi alloys with different C contents and the C04 alloys annealed at 800°C and 1000°C after polarization in a 3.5 wt% NaCl solution is shown in Fig. 6. The images reveal the presence of pitting corrosion and intergranular corrosion on the surfaces of all alloys. The extent of intergranular corrosion on the alloy surface is not consistent. In areas with mild corrosion, only grain boundaries are affected, while in regions with severe corrosion, corrosion products detach and progress deeper, appearing as black lines under metallographic microscopy. For the as-cast C00 alloy (Fig. 6a), numerous non-uniformly distributed pitting pits can be observed, and the corroded grain boundaries display a dendritic morphology. Some grain boundaries appear to be corroded, with the corrosion products falling off and appearing as black lines under the microscope. The corrosion appears to progress in depth (Fig. 6a). As the carbon content increases, the surface morphology of the as-cast C02 and C04 alloys (Figs. 6b and 6c) shows a significant reduction in the number and size of pitting pits. This is attributed to increased nucleation resistance and improved pitting resistance of the alloys. It is worth noting that although intergranular corrosion occurs in the as-cast C04 alloy, the grain boundaries are not easily corroded. This indicates

Table 2

EDS results of the phases in the 1000°C annealed C04 and C08 alloys and the dendrites in the as-cast C00 and C08 alloys. (at%).

Alloys	Regions	Detected composition (at%)					
		Co	Cr	Fe	Mn	Ni	C
1000°C annealed C04	Matrix (FCC)	20.72	19.03	20.36	18.72	21.16	-
	M ₇ C ₃	2.65	51.37	4.93	6.12	2.46	32.47
1000°C annealed C08	Matrix (FCC)	20.16	20.36	19.72	19.72	20.03	-
	M ₇ C ₃	2.74	53.65	3.47	6.95	2.71	30.48
as-cast C00	Dendrite	20.97	21.02	23.29	16.02	18.69	-
	Interdendrite	17.87	17.34	16.61	25.54	22.64	-
as-cast C08	Dendrite	21.38	20.26	22.94	15.70	19.72	-
	Interdendrite	18.79	19.03	18.55	22.56	21.06	-

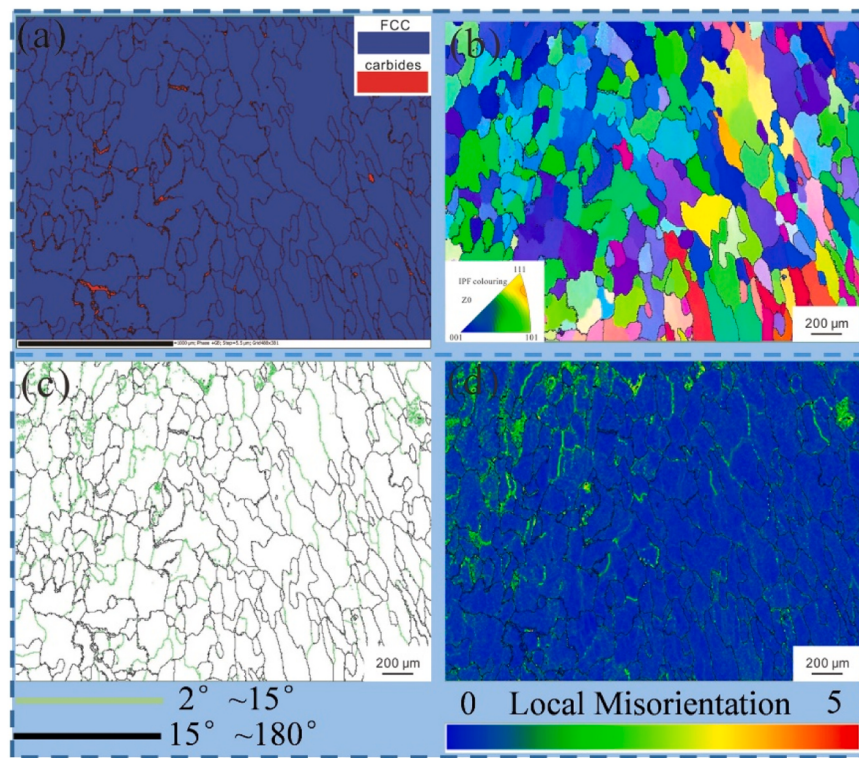


Fig. 4. EBSD images of the 1000°C-120 h annealed C08 alloy. (a) Phase map; (b) IPF+GB; (c) Image quality maps overlaid with high angle boundaries ($\theta \geq 15^\circ$, black color lines) and low angle boundaries ($2^\circ < \theta < 15^\circ$, green lines); (d) Local Misorientation.

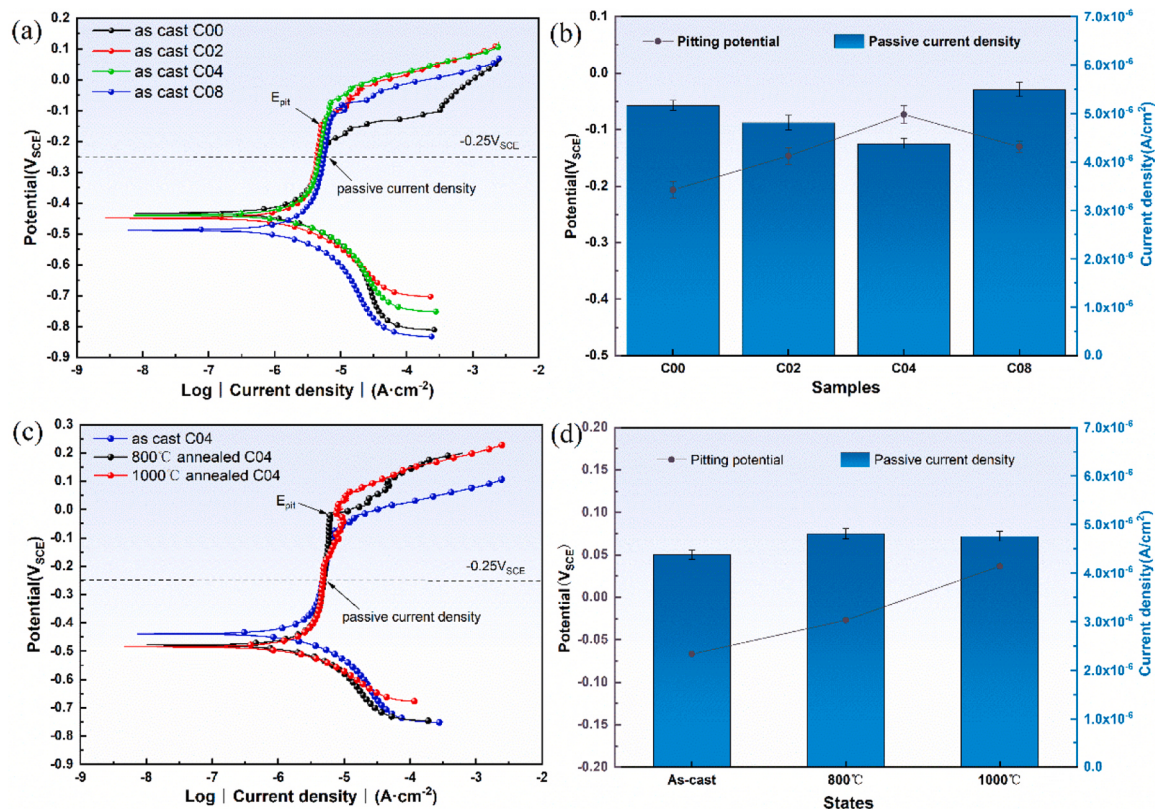


Fig. 5. Polarization curves and their fitted parameters of the CoCrFeMnNiC_x alloys in 3.5 wt% NaCl solution. (a) Polarization curves and (b) their fitted parameters of the as-cast alloys; (c) Polarization curves and (d) their fitted parameters of the annealed CoCrFeMnNiC_x alloys.

Table 3

Electrochemical parameters and their standard deviations for equiatomic CoCrFeMnNi HEA with different carbon contents in 3.5 wt% NaCl solution. E_{corr} : corrosion potential, i_p : passive current density, E_{pit} : critical pitting potential.

State	Samples	E_{corr}/V_{SCE}	$i_{corr} \times 10^{-6} A/cm^2$	E_{pit}/V_{SCE}	$i_p/10^{-6} A/cm^2$
as-cast	C00	-0.43	3.71	-0.2	5.17
	C02	-0.44	2.99	-0.14	4.81
	C04	-0.45	2.54	-0.06	4.38
	C08	-0.48	5.55	-0.13	5.50
800°C annealed	C04	-0.48	1.75	-0.02	4.81
1000°C annealed	C04	-0.48	1.47	0.04	4.76

that the alloy exhibits improved corrosion resistance compared to the other as-cast alloys. The as-cast C08 alloy (Fig. 6d) shows a higher $E_p - E_{corr}$ value than the as-cast C00 alloy, indicating a greater pit nucleation resistance. As a result, there are fewer surface pitting pits on the as-cast C08 alloy. However, the dendrites in the as-cast C08 alloy are thicker, and the intergranular corrosion phenomenon is more pronounced. In some areas, the intergranular corrosion is severe, with corrosion products falling off and progressing along the longitudinal depth.

For the annealed C04 alloy at 800°C and 1000°C (Figs. 6e and 6f), the wider passivation zone and the highest pit nucleation resistance result in almost no noticeable pitting pits on the surface. The size of the few observed pitting pits is also small. Intergranular corrosion is evident, and the grain boundaries are highlighted, consistent with the grain boundaries distribution observed in Fig. 1. The corrosion resistance of the annealed C04 alloy is superior to that of the as-cast C04 alloy.

3.2.2. Electrochemical impedance spectroscopy

The analysis presented in Fig. 7 demonstrates the electrochemical impedance spectroscopy (EIS) results of different carbon content as-cast alloys and annealed C04 alloys at open circuit potential (OCP). The EIS technique measures the corrosion resistance of the alloys by analyzing the charge transfer process and interfacial electrochemical reactions that control the corrosion on their surfaces. The results are shown in the form of Nyquist diagrams, where the arc radius reflects the corrosion resistance of the alloy in the solution [37,38].

From Fig. 7a and Fig. 7c, it is observed that all samples exhibit an

unfinished semi-circular arc, indicating an ongoing corrosion process. The as-cast C04 alloy, with an appropriate carbon content of 0.2 at% and 0.4 at%, shows the largest arc radius, indicating the highest corrosion resistance among the as-cast alloys. This suggests that adding a suitable amount of carbon can effectively enhance the alloy's corrosion resistance. On the other hand, the corrosion resistance of the as-cast C08 alloy decreases due to galvanic corrosion induced by the precipitation of numerous carbides. These results align with those obtained from the polarization curves.

In Fig. 7b, the as-cast C04 alloy exhibits the highest impedance modulus in the low-frequency region, indicating the highest charge transfer resistance among the alloys. Additionally, in Fig. 7d, the θ value approaches -80° in the low and medium frequency range, indicating the formation of a stable passivation film on the alloy surface [39]. The magnitude of $|Z|$ at a frequency of 0.01 Hz characterizes the polarization resistance of the alloy [40]. After annealing at 800°C and 1000°C, the $|Z|$ values of the C04 alloy surpassed those of the as-cast alloy. This indicates that the annealed alloy possesses a more uniform surface, minimal corrosion cell formation, and improved corrosion resistance.

To analyze the passivation and corrosion processes of CoCrFeMnNi alloys, various equivalent circuit models have been employed [41,42]. The corrosion behavior of C-alloyed CoCrFeMnNi alloys is similar to that of C-free alloys. Considering the dispersion effect caused by the inhomogeneity, porosity, and roughness of the passivation film on the sample surface, the capacitance is usually non-ideal, so the CPE is used to replace the pure capacitance element in the EEC Model [43]. The impedance of CPE (Z_{CPE}) can be calculated by Eq. (1):

$$Z_{CPE} = \frac{1}{Q(\omega i)^n} \quad (1)$$

Where Q is the admittance of CPE; ω is angular frequency; i is an imaginary number ($i^2=1$); n is the index of measuring surface inhomogeneity ($-1 \leq n \leq 1$), n=1, 0 and -1 represent a pure capacitance, a pure resistance, and an inductance respectively [44,45].

In the present work, the EEC model used in Ref [6] is employed to fit the EIS results under OCP conditions, as shown in Fig. 7a. The fitting result of the EEC model is found to be satisfactory, as denoted by the $\Sigma\chi^2$ values in Table 4, all of which are lower than 5×10^{-3} . The EEC model parameters include R_s (solution resistance between the working electrode and the reference electrode), R_{ct} (charge transfer resistance), and CPE (double-layer capacitance between the working electrode and the

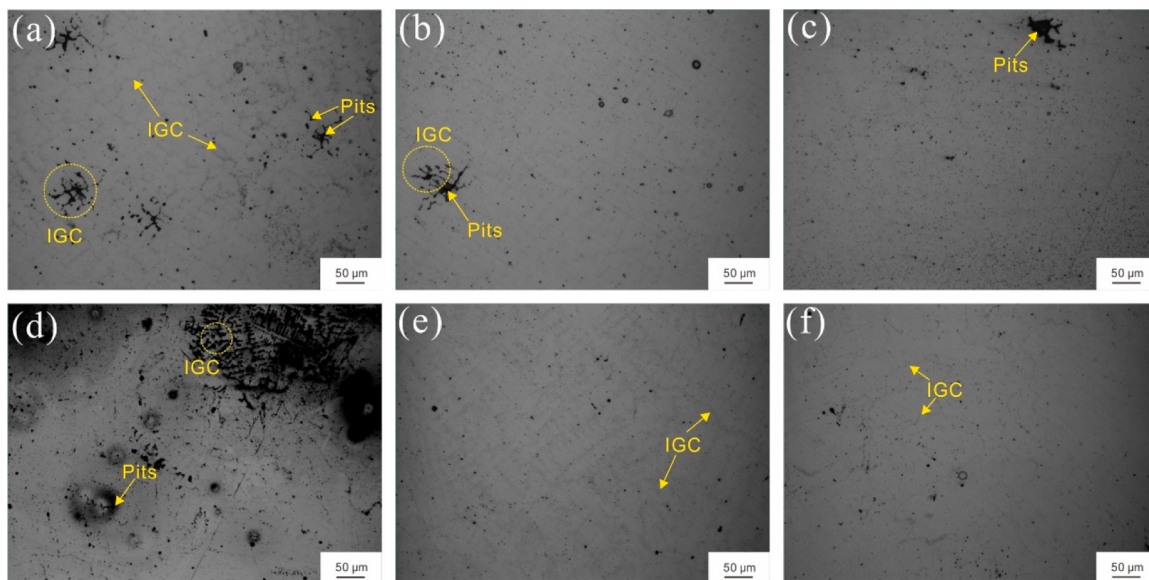


Fig. 6. Surface morphology of the as-cast CoCrFeMnNiC_x HEAs and the annealed C04 alloy after polarization test in 3.5 wt% NaCl solution. (a) as-cast C00; (b) as-cast C02; (c) as-cast C04; (d) as-cast C08; (e) 800°C annealed C04; (f) 1000°C annealed C04.

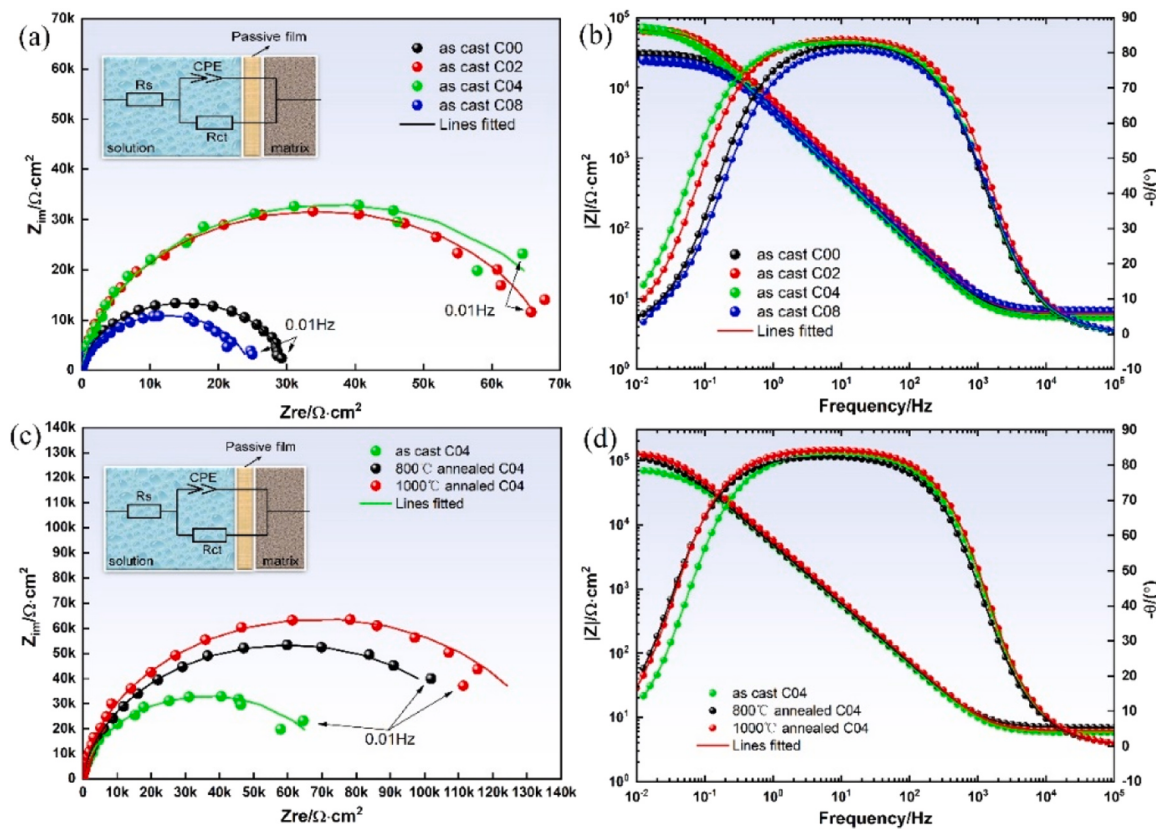


Fig. 7. Electrochemical impedance spectra of the CoCrFeMnNiC_x HEA in 3.5 wt% NaCl. (a) Nyquist, as-cast alloys; (b) Bode plots, as-cast alloys; (c) Nyquist, C04 in different states; (d) Bode plots, C04 in different states.

Table 4

The fitted electrochemical parameters for impedance spectra of the as-cast CoCrFeMnNiC_x HEA with different carbon contents and the annealed C04 in 3.5 wt% NaCl solution.

State	Samples	$R_s/\Omega \cdot \text{cm}^2$	$Q/\Omega^{-1} \text{cm}^{-2} \text{s}^{-n}$	n	$R_{ct}/\Omega \cdot \text{cm}^2$	$\Sigma \chi^2$
as-cast	C00	6.28	3.68×10^{-5}	0.91	2.99×10^4	1.89×10^{-3}
	C02	6.16	3.76×10^{-5}	0.93	6.92×10^4	1.97×10^{-3}
	C04	5.76	3.73×10^{-5}	0.94	7.31×10^4	2.12×10^{-3}
	C08	6.48	3.70×10^{-5}	0.90	2.47×10^4	4.33×10^{-3}
800°C annealed	C04	6.89	3.03×10^{-5}	0.95	1.21×10^5	2.23×10^{-3}
1000°C annealed	C04	6.24	2.82×10^{-5}	0.97	1.39×10^5	2.56×10^{-3}

solution interface). The presence of defective passive films on the alloy surface is indicated by the values of n , which are lower than 1 for all samples. Higher R_{ct} values correspond to slower corrosion rates [46], suggesting that the C04 alloy among the as-cast alloys exhibits the slowest corrosion rate, thereby indicating an improvement in corrosion resistance with the addition of an appropriate amount of carbon.

After annealing at 800°C or 1000°C, the value of n increases, and the capacitance of the electrolyte/corrosion product film interface enhances. This can be attributed to changes in the alloy's microstructure due to annealing, resulting in a more uniform surface state and a relatively dense passive film that enhances the protection of the alloy matrix.

3.2.3. Corrosion morphology and corrosion products after immersion test

To clarify the effect of C and annealing temperature on the corrosion behavior of the alloy, the as-cast alloys with different carbon contents and the C04 alloy annealed at 800°C and 1000°C were immersed in a neutral 3.5 wt% NaCl solution for 30 days. The surface morphology of the alloys was examined, as shown in Fig. 8. It can be observed that thin corrosion product layers are present on the surface of the alloys, and pitting corrosion is more pronounced on some alloy surfaces.

Based on the surface morphology analysis presented in Fig. 6, the corrosion behavior of the alloys primarily involves the coexistence of intergranular corrosion and pitting corrosion. Among the as-cast alloys, the C00 and C08 alloys exhibit more severe pitting corrosion (Fig. 8a and Fig. 8d), indicating lower corrosion resistance. The matrix region in Fig. 8b is an exposed region where the covered corrosion products have peeled off. It is clear that there is no obvious corrosion characteristic in the matrix, which demonstrates that the corrosion product layer provided protection for the matrix. On the other hand, the as-cast C04 alloy shows a denser corrosion product layer and better protective performance (Fig. 8c), which is consistent with the results obtained from the polarization curves and electrochemical impedance spectroscopy. After being annealed at 800°C and 1000°C, alloy C04 exhibits a denser corrosion product layer on its surface and the white corrosion products decreased. This corrosion product layer provides enhanced protection to the underlying matrix (Fig. 8e and Fig. 8f).

EDS mapping in Figs. 8a and 8b shows the distribution of elements on the surface of these alloys is relatively uniform, but it cannot provide a complete understanding of the phase types of the corrosion products. Different phases can be indexed in Raman spectra (Fig. 9) according to Table 5. In the cast alloy, the corrosion products of C00 alloy are FeOOH,

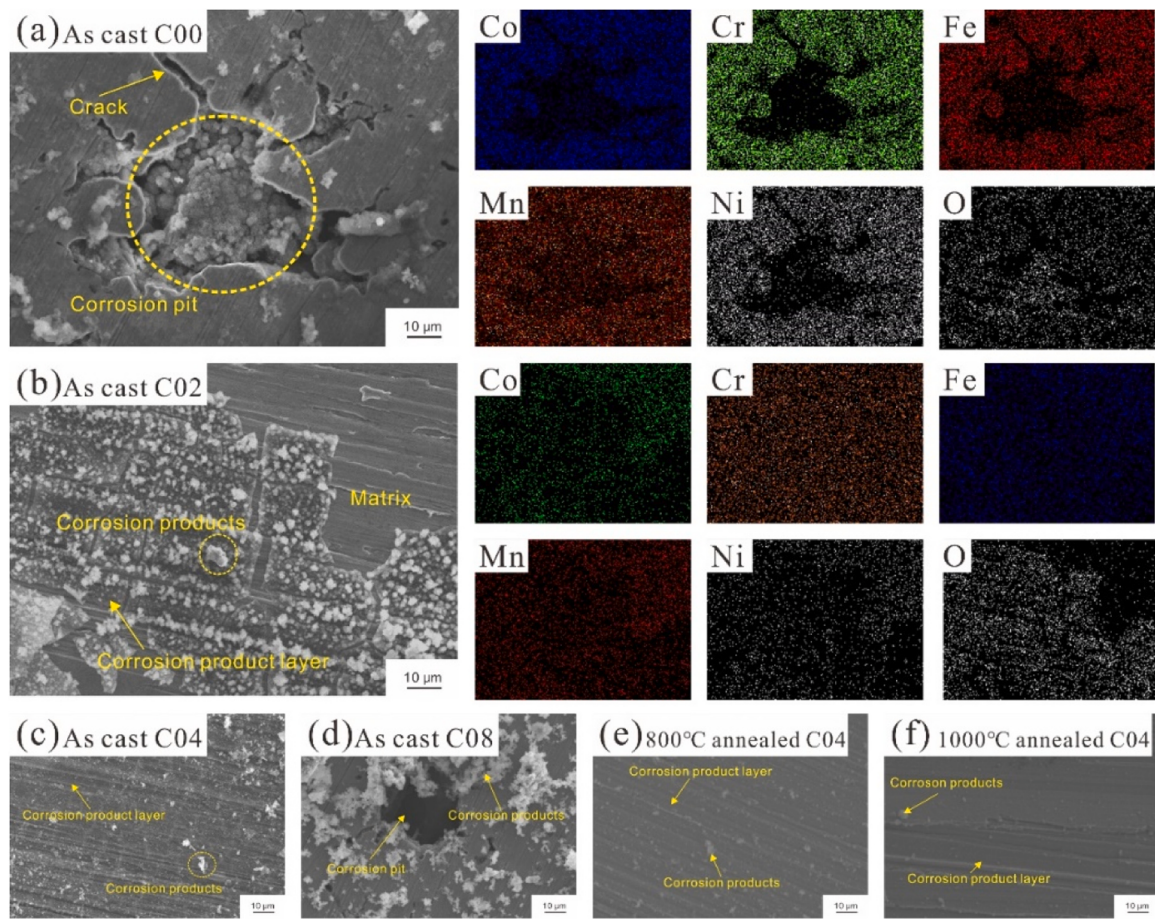


Fig. 8. Surface morphology of the as-cast CoCrFeMnNiC_x HEA and the annealed C04 alloy after immersing in 3.5 wt% NaCl solution. (a) as-cast C00; (b) as-cast C02; (c) as-cast C04; (d) as-cast C08; (e) 800 °C annealed C04; (f) 1000 °C annealed C04.

Fe₂O₃, Cr₂O₃, CrOOH, MnO₂. The corrosion products of C02 alloy are CrOOH, Fe₂O₃. The corrosion products of C04 alloy are Cr₂O₃, Fe₂O₃, NiO. The corrosion products of C08 alloy are FeOOH, Fe₂O₃, MnO₂. The corrosion products of C04 alloy after annealing at 800 °C are Fe₂O₃, Cr₂O₃, NiO, and MnO₂. The corrosion products of C04 alloy after annealing at 1000 °C are Fe₂O₃, Cr₂O₃, MnO₂ and NiO. Based on the analysis of the polarization curves and EIS, the presence of hydroxides in

Table 5

Raman spectroscopy corresponds to the peak positions of each phase in the corrosion products of HEAs.

Phase	Peak position(cm ⁻¹)
Goethite (FeOOH)	208, 244, 299, 402, 482, 550, 681, 997, 1002
Hematite (Fe ₂ O ₃)	226, 297, 355, 422, 498, 561, 610, 654, 809, 1049, 1197
Guyanate (CrOOH)	201, 316, 456, 608, 634, 789, 1158
Eskolaite (Cr ₂ O ₃)	292, 345, 464, 612, 650, 685, 934
Bunsenite (NiO)	178, 206, 243, 400, 552, 719, 864, 1080, 1121
Pyrolusite (MnO ₂)	278, 381, 464, 537, 660, 752, 880, 955

the corrosion products can slightly reduce the corrosion resistance of the alloy.

4. Discussion

4.1. Microstructure formation and evolution mechanism of CoCrFeMnNiC_x alloys

Due to the high entropy effect, the alloys have a higher tendency to form FCC solid solutions rather than intermetallic compounds during the solidification process. When prepared by arc melting, the alloys exhibit typical dendritic structures as shown in Fig. 1. The presence of nonparallel dendrite arms in all alloys can be attributed to component supercooling, as reported in [47]. The microstructure tends to become coarser with the addition of C at certain content [23], as observed in Fig. 1d where the dendrites of the as-cast C08 alloy are thicker than those of the as-cast C00 alloy. It is noteworthy that the addition of C

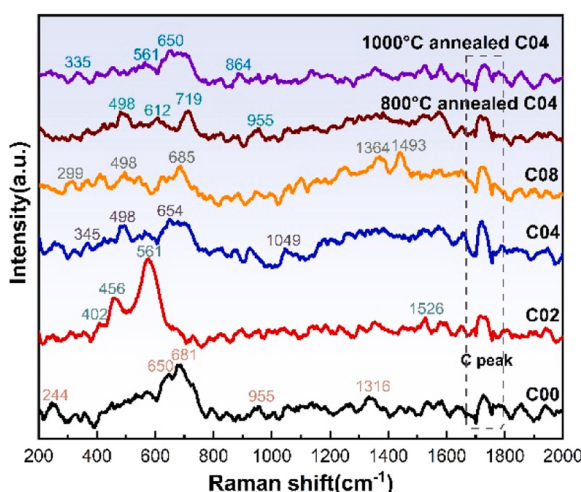


Fig. 9. Raman spectra of the corrosion products of the as-cast CoCrFeMnNiC_x HEA and the 800 or 1000 °C annealed C04 alloy after immersing in 3.5 wt% NaCl solution.

promotes the growth of secondary dendrite arms. In the as-cast C04 alloy, the secondary dendrites are of similar length to the dendrite backbone, resulting in a dense braided network structure. The solubility of C in the FCC matrix is approximately 0.5–0.6 at%, as reported in [48]. However, no carbide precipitation is observed in the as-cast C08 alloy, which may be attributed to the uneven distribution of alloying elements in the as-cast state. The CoCrFeMnNiCx alloys have a strong tendency for element segregation [49,50], where preferential bonding between certain elements and lattice strain effects promote element aggregation [51], as reported in numerous studies [52,53]. Additionally, C tends to segregate at grain boundaries [27,54,55], providing more potential sites for carbide growth. Consequently, it can be observed in Fig. 1 that the carbides at grain boundaries are generally larger in size compared to those inside the grains.

Due to the high cooling rate during solidification, C is likely to be in a non-equilibrium state within the FCC lattice as solution atoms. Heat treatment significantly affects the C content in the FCC solid solution. After annealing at 800°C and 1000°C, the C content in the matrix decreases, and a portion of C combines with alloy elements to form carbides. The high dislocation density at the grain boundaries and dendrites promotes the formation of precipitation points [26,56], hence the observation of carbide precipitation between grain boundaries and dendrites, consistent with other studies [25,27]. The precipitation of carbides has a pinning effect on grain boundary movement, inhibiting grain boundary migration. This is why the grain boundaries of equiaxed grains in the as-cast C04 and as-cast C08 alloys appear relatively tortuous, even exhibiting a zigzag shape. Additionally, the presence of C hinders the diffusion of alloy elements [22], making grain growth and transformation more difficult. The higher the C content, the more pronounced the dendritic segregation phenomenon becomes.

4.2. Corrosion mechanism analysis

As presented above, both intergranular corrosion and pitting corrosion are observed in the as-cast and annealed CoCrFeMnNiCx HEAs, but the formation processes are complex. In a neutral corrosion solution, the dendrite segregation in the as-cast alloy leads to different element enrichment between dendrites (Fig. 3). Conventionally, the chemical segregation in the macro-scale will lead to the occurrence of galvanic corrosion [57]. The dendrite with a higher electrode potential becomes the cathode, while the dendrite with a lower electrode potential becomes the anode, forming a micro-corrosion battery. The anode undergoes corrosion and dissolution. Abundant grain boundaries provide channels for ion dissolution and diffusion, promoting intergranular corrosion. Raman testing confirms the presence of unstable hydroxides in the formed corrosion products [58,59]. Fig. 8 shows defects in the corrosion product film. From this, it can be inferred that defects may allow Cl⁻ to continuously corrode the metal substrate. This leads to the formation of pitting pits on the surface, where Cl⁻ becomes enriched. The concentration difference between the pit and the surrounding area establishes a concentration gradient battery. Through an autocatalytic mechanism, the pitting pits and corroded grain boundaries further develop longitudinally, resulting in the observation of pitting pits and areas where corrosion products have detached on the polarized surface (Fig. 6d). The addition of C affects the alloy's microstructure, influencing its corrosion resistance. The dendrites in the as-cast C02 and as-cast C04 alloys are more compact, and the finer grain structure enhances the diffusion rate of charged particles on the passivation film, improving its ability to passivate [5,60,61]. This weakens the effect of intergranular corrosion due to finer grain boundaries. Thus, the corrosion resistance of the as-cast C02 and as-cast C04 alloys is higher. However, when the C content reaches 0.8 at%, the dendrite spacing increases, making grain boundaries more susceptible to corrosion and damaging the integrity of the passive film on the alloy surface. This aggravates local pitting and decreases the corrosion resistance, and Fig. 8d proves our hypothesis.

After annealing at 800°C and 1000°C, significant changes in the alloy's microstructure occur, resulting in different electrochemical behavior compared to the as-cast alloy. The microstructure of the annealed C04 alloy consists of equiaxed grains with subcrystalline residues, and carbide precipitation is observed on the grain boundaries and within the grains. In a neutral corrosion solution, may constitute galvanic corrosion. The subgrains with high dislocation density and energy become the anode of the corrosion cell, while the grains act as the cathode. Corrosion around carbides can either be due to galvanic coupling between the matrix and the particle or due to a Cr-depletion of the matrix. Galvanic coupling is primarily caused by the potential difference between second phases(without Cr) or between different microstructures. In the intergranular corrosion theory, the precipitation of carbides depletes the Cr element at the grain boundaries and forms a Cr-depleted zone [62]. Consequently, the grain boundaries become the anode, and the grains become the cathode, resulting in intergranular corrosion. Both types of corrosion cells coexist in the HEAs, and the alloy surface is covered with numerous corrosion products. Compared to the passive film on the as-cast alloy, the passive film formed after annealing is denser, improving the protective performance of the matrix, as confirmed by electrochemical impedance spectroscopy analysis. Although carbide precipitation is observed in the C04 alloy annealed at 1000°C, its corrosion resistance is still the highest. This can be attributed to the unstable subcrystalline structure. After annealing at 1000°C, the microstructure of the C04 alloy is very similar to that of the C08 alloy, both exhibiting the presence of subgrains and carbides. Therefore, it is reasonable to infer relevant information about the microstructural characteristics of the C04 alloy from the EBSD results of the C08 alloy.in Fig. 4. Fig. 4d shows that the presence of subcrystalline structures results in significant orientation differences within the grain, creating preferred paths for corrosion propagation [63]. Furthermore, low-angle grain boundaries (LAGB) are more prone to significant dislocation interactions than high-angle grain boundaries (HAGB) (Fig. 4c). Dislocations can affect corrosion resistance by influencing the local electrochemical environment and generating local galvanic couples, leading to accelerated corrosion at dislocation sites [64,65]. Therefore, the rapid dissolution of these positions in the corrosion solution provides favorable conditions for the passivation of the alloy. The corrosion products effectively cover the alloy matrix, providing effective protection. Pitting pits may arise from the loss of some carbides from the matrix in rapidly dissolving regions. The pitting pits on the surface of the C04 alloy annealed at 1000°C are very small due to the resistance to pit nucleation.

5. Conclusion

The present study systematically investigated the influences of carbon alloying and annealing temperature on the microstructure and corrosion behavior of CoCrFeMnNiCx HEAs in a 3.5 wt% NaCl solution. Based on the findings, the following conclusions can be drawn:

- 1) In the as-cast state, the addition of carbon had a refining effect on the dendrite structure. This refining effect became more apparent with increasing carbon content from 0 at% to 0.4 at%, but the dendrites coarsened as the carbon content further increased to 0.8 at%. Notably, the alloy containing 0.4 at% carbon exhibited the most significant microstructure refinement.
- 2) After annealing at 800°C, the dendrite structure transitioned into equiaxed grains truncated by coarse grain boundaries. The presence of residual subcrystals within the equiaxed grains became more evident with an increase in carbon content from 0 at% to 0.8 at%. After annealing at 1000°C, only alloys containing 0.4 at% and 0.8 at % C observed subgrain residues, accompanied by carbide precipitation.
- 3) In a 3.5 wt% NaCl solution, the presence of C in the as-cast alloy improved its passivation ability and enhanced its pitting corrosion

- resistance compared to the CoCrFeMnNi HEA. Furthermore, the corrosion resistance of the alloy containing 0.4 at% C increased with higher annealing temperatures. The highest corrosion resistance was observed in the 1000°C annealed state.
- 4) Both intergranular corrosion and pitting corrosion were observed in the as-cast and annealed alloys. The presence of 0–0.4 at% C weakened the pitting behavior, resulting in a reduction in the size and number of pitting pits on the alloy surface. However, the pitting behavior was enhanced again in the alloy containing 0.8 at% C. The alloys containing 0.4 at% C exhibited predominant intergranular corrosion after annealing at 800°C and 1000°C.
- CRediT authorship contribution statement**
- Haoping Peng:** Funding acquisition. **Xuping Su:** Methodology. **Xiangying Zhu:** Conceptualization. **Fucheng Zhu:** Writing – original draft, Investigation, Data curation. **Ya Liu:** Writing – review & editing, Validation. **Changjun Wu:** Writing – review & editing, Project administration, Conceptualization.
- Declaration of Competing Interest**
- The authors declare that they have no known competing financial interests or personal relationships that could have appeared to influence the work reported in this paper.
- Data availability**
- Data will be made available on request.
- Acknowledgment**
- This study was supported by the National Natural Science Foundation of China (52271005, 51971039) and the Postgraduate Research & Practice Innovation Program of Jiangsu Province (SJCX23_1479).
- References**
- [1] J.W. Yeh, S.K. Chen, S.J. Lin, J.Y. Gan, T.S. Chin, T.T. Shun, C.H. Tsau, S.Y. Chang, Nanostructured high-entropy alloys with multiple principal elements: novel alloy design concepts and outcomes, *Adv. Eng. Mater.* 6 (2004) 299–303, <https://doi.org/10.1002/ad-em.200300567>.
 - [2] M. Slobodyan, E. Pesterev, A. Markov, Recent advances and outstanding challenges for implementation of high entropy alloys as structural materials, *Mater. Today Commun.* 36 (2023) 106422, <https://doi.org/10.1016/j.mtcomm.2023.106422>.
 - [3] Z. Zhang, M.M. Mao, J. Wang, B. Gludovatz, Z. Zhang, S.X. Mao, E.P. George, Q. Yu, R.O. Ritchie, Nanoscale origins of the damage tolerance of the high-entropy alloy CrMnFeCoNi, *Nat. Commun.* 6 (2015) 10143, <https://doi.org/10.1038/ncomms10143>.
 - [4] T.N. Lam, M.Y. Luo, T. Kawasaki, S. Harjo, J. Jain, S.Y. Lee, A.C. Yeh, E.W. Huang, Tensile response of as-cast CoCrFeNi and CoCrFeMnNi high-entropy alloys, *Crystals* 12 (2022) 157, <https://doi.org/10.3390/cryst12020157>.
 - [5] H. Shimizu, M. Yuasa, H. Miyamoto, K. Edalati, Corrosion behavior of ultrafine-grained CoCrFeMnNi high-entropy alloys fabricated by high-pressure torsion, *Mater. (Basel)* 15 (2022) 1007, <https://doi.org/10.3390/ma15031007>.
 - [6] J.P. Wang, Z. Zhang, H.L. Dai, H. Fujiwara, X. Chen, K. Ameyama, Enhanced corrosion resistance of CoCrFeMnNi high entropy alloy using heterogeneous structure design, *Corros. Sci.* 209 (2022) 110761, <https://doi.org/10.1016/j.corsci.2022.110761>.
 - [7] J.K. Xiao, H. Tan, Y.-Q. Wu, J. Chen, C. Zhang, Microstructure and wear behavior of FeCoNiCrMn high entropy alloy coating deposited by plasma spraying, *Surf. Coat. Tech.* 385 (2020) 125430, <https://doi.org/10.1016/j.surcoat.2020.125430>.
 - [8] A. Ayyagari, C. Barthelemy, B. Gwalani, R. Banerjee, T.W. Scharf, S. Mukherjee, Reciprocating sliding wear behavior of high entropy alloys in dry and marine environments, *Mater. Chem. Phys.* 210 (2018) 162–169, <https://doi.org/10.1016/j.matchemphys.2017.07.031>.
 - [9] H. Feng, H.B. Li, J. Dai, Y. Han, J.D. Qu, Z.H. Jiang, Y. Zhao, T. Zhang, Why CoCrFeMnNi HEA could not passivate in chloride solution? A novel strategy to significantly improve corrosion resistance of CoCrFeMnNi HEA by N-alloying, *Corros. Sci.* 204 (2022) 110396, <https://doi.org/10.1016/j.corsci.2022>.
 - [10] M.A. Hassan, I.M. Ghayad, A.S.A. Mohamed, A.E. El-Nikhaily, O.A. Elkady, Improvement ductility and corrosion resistance of CoCrFeNi and AlCoCrFeNi HEAs by electroless copper technique, *J. Mater. Res. Technol.* 13 (2021) 463–485, <https://doi.org/10.1016/j.jmrt.20-21.04.083>.
 - [11] C.W. Lu, Y.S. Lu, Z.H. Lai, H.W. Yen, Y.L. Lee, Comparative corrosion behavior of Fe50Mn30Co10Cr10 dual-phase high-entropy alloy and CoCrFeMnNi high-entropy alloy in 3.5 wt% NaCl solution, *J. Alloy. Compd.* 842 (2020) 155824, <https://doi.org/10.1016/j.jallcom.2020.155824>.
 - [12] H. Luo, Z. Li, A.M. Mingers, D. Raabe, Corrosion behavior of an equiatomic CoCrFeMnNi high-entropy alloy compared with 304 stainless steel in sulfuric acid solution, *Corros. Sci.* 134 (2018) 131–139, <https://doi.org/10.1016/j.corsci.2018.02.031>.
 - [13] T. Aiso, M. Nishimoto, I. Muto, Y. Sugawara, Roles of alloying elements in the corrosion resistance of equiatomic CoCrFeMnNi high-entropy alloy and application to corrosion-resistant alloy design, *Mater. Trans.* 62 (2021) 1677–1680, <https://doi.org/10.2320/mater-trans.MT2021136>.
 - [14] N. Meena, G. Gunasekaran, P. Veeriah, A.G. Rao, N. Prabhu, Corrosion behaviour of friction stir processed, metastable, dual-phase, Fe49.5Mn30Co10Cr10C0.5, multi-principal element alloy, *J. Alloy. Compd.* 952 (2023) 169967, <https://doi.org/10.1016/j.jallcom.2023.169967>.
 - [15] H. Dai, S. Shi, L. Yang, J. Hu, C. Liu, C. Guo, X. Chen, Effects of elemental composition and microstructure inhomogeneity on the corrosion behavior of nickel-based alloys in hydrofluoric acid solution, *Corros. Sci.* 176 (2020) 108917, <https://doi.org/10.1016/j.corsci.2020.108917>.
 - [16] A. Rodriguez, J.H. Tylickzak, M. Ziomek-Moroz, Corrosion behavior of CoCrFeMnNi high-entropy alloys (HEAs) under aqueous acidic conditions, *ECS Trans.* 77 (2017) 741, <https://doi.org/10.1149/07711.0741ecst>.
 - [17] M.Y. He, Y.F. Shen, N. Jia, P.K. Liaw, C and N doping in high-entropy alloys: a pathway to achieve desired strength-ductility synergy, *Appl. Mater. Today* 25 (2021) 101162, <https://doi.org/10.1016/j.apmt.2021.101162>.
 - [18] Y. Chen, Q. Zhao, H. Wu, Q. Fang, J. Li, Effect of interstitial N atom on physical and mechanical properties of FeCoCrNiMn high-entropy alloys: a first-principles study, *Phys. B* 615 (2021) 413078, <https://doi.org/10.1016/j.physb.2021.413078>.
 - [19] H. Song, M. Yu, Y. Zhang, W. Zhang, Z. Liu, F. Zhang, F. Tian, First-principle study of interstitial atoms (C, B and Si) in CrFeCoNi high entropy alloy, *Mater. Today Commun.* 31 (2022) 103241, <https://doi.org/10.1016/j.mtcomm.2022.103241>.
 - [20] B. Kang, T. Kong, N.H. Dan, D.D. Phuong, H.J. Ryu, S.H. Hong, Effect of boron addition on the microstructure and mechanical properties of refractory Al0.1CrNbVMo high-entropy alloy, *Int. J. Refract. Met. H.* 100 (2021) 105636, <https://doi.org/10.1016/j.ijrmhm.2021.105636>.
 - [21] J. Li, B. Gao, S. Tang, B. Liu, Y. Liu, Y. Wang, J. Wang, High temperature deformation behavior of carbon-containing FeCoCrNiMn high entropy alloy, *J. Alloy. Compd.* 747 (2018) 571–579, <https://doi.org/10.1016/j.jallcom.2018.02.332>.
 - [22] J. Li, B. Gao, Y. Wang, X. Chen, Y. Xin, S. Tang, B. Liu, Y. Liu, M. Song, Microstructures and mechanical properties of nano carbides reinforced CoCrFeMnNi high entropy alloys, *J. Alloy. Compd.* 792 (2019) 170–179, <https://doi.org/10.1016/j.jallcom.2019.03.403>.
 - [23] R. Ravi, S.R. Bakshi, Microstructural evolution and wear behavior of carbon added CoCrFeMnNi multi-component alloy fabricated by mechanical alloying and spark plasma sintering, *J. Alloy. Compd.* 883 (2021) 160879, <https://doi.org/10.1016/j.jallcom.2021.160879>.
 - [24] J.K. Xiao, H. Tan, J. Chen, A. Martini, C. Zhang, Effect of carbon content on microstructure, hardness and wear resistance of CoCrFeMnNiCx high-entropy alloys, *J. Alloy. Compd.* 847 (2020) 156533, <https://doi.org/10.1016/j.jallcom.2020.156533>.
 - [25] N.D. Stepanov, N.Y. Yurchenko, M.A. Tikhonovsky, G.A. Salishchev, Effect of carbon content and annealing on structure and hardness of the CoCrFeNiMn-based high entropy alloys, *J. Alloy. Compd.* 687 (2016) 59–71, <https://doi.org/10.1016/j.jallcom.2016.06.103>.
 - [26] J.Y. Ko, S.I. Hong, Microstructural evolution and mechanical performance of carbon-containing CoCrFeMnNi-C high entropy alloys, *J. Alloy. Compd.* 743 (2018) 115–125, <https://doi.org/10.1016/j.jallcom.2018.01.348>.
 - [27] J. Chen, Z. Yao, X. Wang, Y. Lu, X. Wang, Y. Liu, X. Fan, Effect of C content on microstructure and tensile properties of as-cast CoCrFeMnNi high entropy alloy, *Mater. Chem. Phys.* 210 (2018) 136–145, <https://doi.org/10.1016/j.matchemphys.2017.08.011>.
 - [28] I. Baker, Interstitial strengthening in f.c.c. metals and alloys, *Adv. Powd. Mater.* 1 (2022) 100034, <https://doi.org/10.1016/j.apmat.2022.100034>.
 - [29] H. Luo, S. Zou, Y.H. Chen, Z. Li, C. Du, X. Li, Influence of carbon on the corrosion behaviour of interstitial equiatomic CoCrFeMnNi high-entropy alloys in a chlorinated concrete solution, *Corros. Sci.* 163 (2020) 108287, <https://doi.org/10.1016/j.corsci.2019.108287>.
 - [30] E.M. Paschalidou, R. Lindblad, L.Z. Medina, D. Karlsson, U. Jansson, L. Nyholm, Corrosion studies on multicomponent CoCrFeMnNi(C) thin films in acidic environments, *Electro Acta* 404 (2022) 139756, <https://doi.org/10.1016/j.electacta.2021.139756>.
 - [31] L.Z. Medina, M.V.T. da Costa, E.M. Paschalidou, G. Lindwall, L. Riekehr, M. Korvela, S. Fritze, S. Kolozsvari, E.K. Gamstedt, L. Nyholm, U. Jansson, Enhancing corrosion resistance, hardness, and crack resistance in magnetron sputtered high entropy CoCrFeMnNi coatings by adding carbon, *Mater. Des.* 205 (2021) 109711, <https://doi.org/10.1016/j.mat-des.2021.109711>.
 - [32] T. Huang, L. Jiang, C. Zhang, H. Jiang, Y. Lu, T. Li, Effect of carbon addition on the microstructure and mechanical properties of CoCrFeNi high entropy alloy, *Sci. China Technol. Sc.* 61 (2018) 117–123, <https://doi.org/10.1007/s11431-017-9134-6>.
 - [33] M.V. Klimova, A.O. Semenyuk, D.G. Shaysultanov, G.A. Salishchev, S. V. Zhurebtsov, N.D. Stepanov, Effect of carbon on cryogenic tensile behavior of CoCrFeMnNi-type high entropy alloys, *J. Alloy Compd.* 811 (2019) 152000, <https://doi.org/10.1016/j.jallcom.2019.152000>.

- [34] H.P. Peng, Z.H. Lin, R.D. Li, P.D. Niu, Z.J. Zhang, Corrosion behavior of an equiatomic CoCrFeMnNi high-entropy alloy- a comparison between selective laser melting and cast, *Front. Mater.* 7 (2020) 00244, <https://doi.org/10.3389/fmats.2020.00244>.
- [35] S. Khireche, D. Bougrara, A. Kadri, L. Hamadou, N. Benbrahim, Corrosion mechanism of Al, Al-Zn and Al-Zn-Sn alloys in 3wt% NaCl solution, *Corros. Sci.* 87 (2014) 504–516, <https://doi.org/10.1016/j.corsci.2014.07.018>.
- [36] A. Pardo, M.C. Merino, A.E. Coy, F. Viejo, R. Arrabal, E. Matykina, Pitting corrosion behaviour of austenitic stainless steels – combining effects of Mn and Mo additions, *Corros. Sci.* 50 (2008) 1796–1806, <https://doi.org/10.1016/j.corsci.2008.04.005>.
- [37] C.N. Cao, On the impedance plane displays for irreversible electrode reactions based on the stability conditions of the steady-state—I. One state variable besides electrode potential, *Electrochim. Acta* 35 (1990) 831–836, [https://doi.org/10.1016/0013-4686\(90\)90077-D](https://doi.org/10.1016/0013-4686(90)90077-D).
- [38] H. Feng, H.B. Li, Z.-H. Jiang, T. Zhang, N. Dong, S.-C. Zhang, P.-D. Han, S. Zhao, Z.-G. Chen, Designing for high corrosion-resistant high nitrogen martensitic stainless steel based on DFT calculation and pressurized metallurgy method, *Corros. Sci.* 158 (2019) 108081, <https://doi.org/10.1016/j.corsci.2019.07.007>.
- [39] H. Luo, S. Gao, C. Dong, X. Li, Characterization of electrochemical and passive behaviour of Alloy 59 in acid solution, *Electrochim. Acta* 135 (2014) 412–419, <https://doi.org/10.1016/j.elect-acta.2014.04.128>.
- [40] C.A. Della Rovere, J.H. Alano, R. Silva, P.A.P. Nascente, J. Otubo, S.E. Kuri, Characterization of passive films on shape memory stainless steels, *Corros. Sci.* 57 (2012) 154–161, <https://doi.org/10.1016/j.corsci.2011.12.022>.
- [41] J. Ren, C. Mahajan, L. Liu, D. Follette, W. Chen, S. Mukherjee, Corrosion behavior of selectively laser melted CoCrFeMnNi high entropy alloy, *Metals* 9 (2019) 1029, <https://doi.org/10.3390/met9101029>.
- [42] Z. Xu, H. Zhang, X. Du, Y. He, H. Luo, G. Song, L. Mao, T. Zhou, L. Wang, Corrosion resistance enhancement of CoCrFeMnNi high-entropy alloy fabricated by additive manufacturing, *Corros. Sci.* 177 (2020) 108954, <https://doi.org/10.1016/j.corsci.2020.108954>.
- [43] M. BenSalah, R. Sabot, E. Triki, L. Dhouib, P. Refait, M. Jeannin, Passivity of Sanicro28 (UNS N-08028) stainless steel in polluted phosphoric acid at different temperatures studied by electrochemical impedance spectroscopy and Mott-Schottky analysis, *Corros. Sci.* 86 (2014) 61–70, <https://doi.org/10.1016/j.corsci.2014.04.056>.
- [44] P.K. Rai, S. Shekhar, K. Mondal, Development of gradient microstructure in mild steel and grain size dependence of its electrochemical response, *Corros. Sci.* 138 (2018) 85–95, <https://doi.org/10.1016/j.corsci.2018.04.009>.
- [45] J. Yang, Y. Lu, Z. Guo, J. Gu, C. Gu, Corrosion behaviour of a quenched and partitioned medium carbon steel in 3.5wt% NaCl solution, *Corros. Sci.* 130 (2018) 64–75, <https://doi.org/10.1016/j.corsci.2017.10.027>.
- [46] D. Song, A. Ma, W. Sun, J. Jiang, J. Jiang, D. Yang, G. Guo, Improved corrosion resistance in simulated concrete pore solution of surface nanocrystallized rebar fabricated by wire-brushing, *Corros. Sci.* 82 (2014) 437–441, <https://doi.org/10.1016/j.corsci.2014.01.034>.
- [47] S.G. Ma, P.K. Liaw, M.C. Gao, J.W. Qiao, Z.H. Wang, Y. Zhang, Damping behavior of Al_xCoCrFeNi high-entropy alloys by a dynamic mechanical analyzer, *J. Alloy Compd.* 604 (2014) 331–339, <https://doi.org/10.1016/j.jallcom.2014.03.050>.
- [48] Z. Wu, C.M. Parish, H. Bei, Nano-twin mediated plasticity in carbon-containing FeNiCoCrMn high entropy alloys, *J. Alloy Compd.* 647 (2015) 815–822, <https://doi.org/10.1016/j.jall-com.2015.05.224>.
- [49] G.A. Salishchev, M.A. Tikhonovsky, D.G. Shaysultanov, N.D. Stepanov, A. V. Kuznetsov, I.V. Kolodiy, A.S. Tortika, O.N. Senkov, Effect of Mn and V on structure and mechanical properties of high-entropy alloys based on CoCrFeNi system, *J. Alloy Compd.* 591 (2014) 11–12, <https://doi.org/10.1016/j.jallcom.2013.12.210>.
- [50] M. Laurent-Brocq, A. Akhatova, L. Perriere, S. Chebini, X. Sauvage, E. Leroy, Y. Champion, Insights into the phase diagram of the CrMnFeCoNi high entropy alloy, *Acta Mater.* 88 (2015) 355–365, <https://doi.org/10.1016/j.actamat.2015.01.068>.
- [51] Q.J. Li, H. Sheng, E. Ma, Strengthening in multi-principal element alloys with local-chemical-order roughened dislocation pathways, *Nat. Commun.* 10 (2019) 3563, <https://doi.org/10.1038/s41467-019-11464-7>.
- [52] B. Cantor, I. Chang, P. Knight, A. Vincent, Microstructural development in equiatomic multicomponent alloys, *Mat. Sci. Eng. A-Struct.* 375 (2004) 213–218, <https://doi.org/10.1016/j.msea.2003.10.257>.
- [53] N. Stepanov, M. Tikhonovsky, N. Yurchenko, D. Zyabkin, M. Klimova, S. Zhrebtssov, A. Efimov, G. Salishchev, Effect of cryo-deformation on structure and properties of CoCrFeNiMn high-entropy alloy, *Intermetallics* 59 (2015) 8–17, <https://doi.org/10.1016/j.intermet.2014.12.004>.
- [54] J.F. Nie, Y.M. Zhu, J.Z. Liu, X.Y. Fang, Periodic segregation of solute atoms in fully coherent twin boundaries, *Science* 340 (2013) 957–960, <https://doi.org/10.1126/science.1229369>.
- [55] J. Chen, Z. Wang, X. Ma, X. Wang, Y. Lei, W. Yan, Annealing strengthening of pre-deformed Mg-10Gd-3Y-0.3Zr alloy, *J. Alloy Compd.* 642 (2015) 92–97, <https://doi.org/10.1016/j.jall-com.2015.04.102>.
- [56] N.D. Stepanov, D.G. Shaysultanov, R.S. Chernichenko, N.Y. Yurchenko, S. V. Zhrebtssov, M.A. Tikhonovsky, G.A. Salishchev, Effect of thermomechanical processing on microstructure and mechanical properties of the carbon-containing CoCrFeNiMn high entropy alloy, *J. Alloy Compd.* 693 (2017) 394–405, <https://doi.org/10.1016/j.jallcom.2016.09.208>.
- [57] R. Zhou, W. Chen, W. Li, T.H. Chou, Y.H. Chen, X. Liang, J. Luan, Y. Zhu, J. C. Huang, Y. Liu, 3D printed N-doped CoCrFeNi high entropy alloy with more than doubled corrosion resistance in dilute sulphuric acid, *NPJ, Mat. Degrad.* 7 (2023) 8, <https://doi.org/10.1038/s41529-023-00320-1>.
- [58] B.J. Wang, D.K. Xu, J. Sun, E.-H. Han, Effect of grain structure on the stress corrosion cracking (SCC) behavior of an as-extruded Mg-Zn-Zr alloy, *Corros. Sci.* 157 (2019) 347–356, <https://doi.org/10.1016/j.corsci.2019.06.017>.
- [59] S.S. Nene, M. Frank, K. Liu, S. Sinha, R.S. Mishra, B.A. McWilliams, K.C. Cho, Corrosion-resistant high entropy alloy with high strength and ductility, *Scr. Mater.* 166 (2019) 168–172, <https://doi.org/10.1016/j.scriptamat.2019.03.028>.
- [60] Y. Wang, J.S. Jin, M. Zhang, X.Y. Wang, P. Gong, J.C. Zhang, J.C. Liu, Effect of the grain size on the corrosion behavior of CoCrFeMnNi HEAs in a 0.5 M H₂SO₄ solution, *J. Alloy Compd.* 858 (2021) 157712, <https://doi.org/10.1016/j.jallcom.2020.157712>.
- [61] Z. Zhang, X. Li, H. Yi, H. Xie, Z. Zhao, P. Bai, Clarify the role of Nb alloying on passive film and corrosion behavior of CoCrFeMnNi high entropy alloy fabricated by laser powder bed fusion, *Corros. Sci.* 224 (2023) 111510, <https://doi.org/10.1016/j.corsci.2023.111510>.
- [62] M.P. Ryan, D.E. Williams, R.J. Chater, B.M. Hutton, D.S. McPhail, Why stainless steel corrodes, *Nature* 415 (2002) 770–774, <https://doi.org/10.1038/415770a>.
- [63] R. Zhang, Y. Qiu, Y. Qi, N. Birbilis, A closer inspection of a grain boundary immune to intergranular corrosion in a sensitised Al-Mg alloy, *Corros. Sci.* 133 (2018) 1–5, <https://doi.org/10.1016/j.corsci.2018.01.009>.
- [64] S. Son, J. Kwak, J. Lee, F. Haftlang, Y.-T. Kim, H.S. Kim, Exceptional combination of mechanical and corrosion properties in partially recrystallized CoCrFeNiMo medium-entropy alloys, *J. Mater. Res. Technol.* 25 (2023) 5136–5147, <https://doi.org/10.1016/j.jmrt.2023.07.007>.
- [65] C. Liu, R.I. Revilla, X. Li, Z. Jiang, S. Yang, Z. Cui, D. Zhang, H. Terryn, X. Li, New insights into the mechanism of localised corrosion induced by TiN-containing inclusions in high strength low alloy steel, *J. Mater. Res. Technol.* 124 (2022) 141–149, <https://doi.org/10.1016/j.jmst.2021.12.075>.